Journal of
Materials Chemistry A

Accepted Manuscript

This article can be cited before page numbers have been issued, to do this please use: B. Liu, I. Mosa, W. Song, H. Zheng, C. Kuo, J. F. Rusling, S. L. Suib and J. He, *J. Mater. Chem. A*, 2016, DOI: 10.1039/C6TA02017H.

ROYAL SOCIETY OF CHEMISTRY

www.rsc.org/materialsA

View Article Online
DOI: 10.1039/C6TA02017H

Journal Name

ARTICLE

Unconventional structural and morphological transitions of nanosheets, nanoflakes and nanorods of AuNP@MnO_2

Received 00th January 20xx,
Accepted 00th January 20xx

DOI: 10.1039/x0xx00000x

www.rsc.org/

Ben Liu,[a] Islam M. Mosa,[a,b] Wenqiao Song,[a] Haoquan Zheng,[c] Chung-Hao Kuo,[a] James F. Rusling,[a,d] Steven L. Suib,*[a,d] and Jie He*[a,d]

Two-dimensional (2-D) layered inorganic materials with ultra-high surface area and mechanical strength have shown impressive photo-/electro-catalytic activities. We herein report a facile synthetic strategy to grow monodispersed 2-D MnO_2 nanosheet on an individual gold nanoparticle (AuNP@MnO_2 nanosheet), and demonstrate that the strongly interacted AuNP and MnO_2 nanosheet could greatly improve the electrocatalytic activity of the MnO_x family for electrocatalytic oxygen reduction reactions (ORRs). AuNP@MnO_2 nanosheets were prepared using a hydrothermal reduction of $KMnO_4$ by citrate ligands capped on AuNPs. Because of the metastability of the layered MnO_2 nanosheets, we observed unconventional structural and morphological transitions of amorphous MnO_2 nanosheets to δ-MnO_2 nanoflakes, and eventually to α-MnO_2 nanorods under hydrothermal conditions. The layered MnO_2 nanosheets underwent a structural expansion to nanoflakes before the curling and re-folding of layered MnO_2 nanosheets occurred. *The intermediate states and structural transitions via a "layer compression", for the first time, were experimentally recorded at a single-NP scale using electron microscopy*. Moreover, we found the electrocatalytic activity of AuNP@MnO_2 nanosheets was enhanced roughly 30-40 times, compared to that of pure MnO_2 nanosheets and AuNPs. The strong interaction of metal-oxide interfaces (MnO_2 nanosheets and AuNPs) was likely responsible for the improved electrocatalytic activity. This interaction of MnO_2 and AuNPs was weakened in the course of hydrothermal treatment where partially positively charged Au^+ was reduced at elevated temperatures, accompanying with the decrease of ORR activity. This insight into the effect of topological nanostructures and metal-oxide interactions on the electrocatalytic performance of the MnO_x family is believed to illustrate an alternative pathway to develop new efficient electrocatalysts.

1. Introduction

The latest development of two-dimensional (2-D) layered inorganic materials with a thickness of a few nanometers or less and a lateral size ranging from hundreds of nanometers to a few centimeters has largely advanced various types of novel catalysts.[1-4] In particular, 2-D layered materials with ultra-high surface areas and mechanical strengths have been extensively utilized as photo-/electro-catalysts directly or as supports.[5-11] A boost in catalytic activity was reported for many systems, *e.g.* nitrogen-doped graphene,[5] cobalt oxide/graphene hybrids[9] and Ni-Fe layered double hydroxides.[10] Of over 30 polymorphs, Birnessite (or δ-MnO_2) is a 2-D layered MnO_x with edge-shared MnO_6 octahedra filled with metal ions and a single layer of water in between layers.[12] Sasaki *et al.* first reported that the intercalation and chemical exfoliation of δ-MnO_2 in the presence of tetrabutylammonium hydroxide could yield 2-D unilamellar nanosheets of MnO_2.[13] Recently, a bottom-up wet-chemical synthesis was developed by utilizing a direct reduction of $KMnO_4$.[14-18] Because of their accessible high surface area, MnO_2 nanosheets showed improved electrochemical performance for Li-ion batteries and supercapacitors, compared to other MnO_x species.[19-21] Alternatively, MnO_2 nanosheets, similar to layered δ-MnO_2, are metastable;[22-25] and they can transform into other polymorphs (*e.g.* nanowires of α-MnO_2) by rolling and restacking with cations and water.[22] However, a direct observation of this morphological and structural transition of MnO_2, as well as the intermediate states, is very challenging and has been rarely explored.

We herein report a direct observation of the morphological and structural transition of MnO_2 nanosheets grown on gold nanoparticles (denoted as AuNP@MnO_2 nanosheets hereafter). AuNP@MnO_2 nanosheets composed of metallic AuNP core and MnO_2 nanosheet shell were prepared via a direct hydrothermal reduction of $KMnO_4$. Because of the metastability of layered MnO_2 nanosheets, unconventional structural and morphological transitions of amorphous MnO_2 nanosheets to α-MnO_2 nanorods under hydrothermal

[a] Department of Chemistry, University of Connecticut, Storrs, Connecticut, 06269 Emails: steven.suib@uconn.edu (SLS) and jie.he@uconn.edu (JH)
[b] Department of Chemistry, Tanta University, Tanta, 31527, Egypt.
[c] Berzelii Center EXSELENT on Porous Materials, Department of Materials and Environmental Chemistry, Stockholm University, Stockholm, Sweden, 10691.
[d] Institute of Materials Science, University of Connecticut, Storrs, Connecticut, 06269, USA.

†Electronic Supplementary Information (ESI) available: Experimental details, and more characterizations and electrocatalytic results of AuNP@MnO_2. See DOI: 10.1039/x0xx00000x

View Article Online
DOI: 10.1039/C6TA02017H

conditions were directly observed using electron microscopy. Layered MnO_2 nanosheets were "visualized", for the first time, to undergo a morphological expansion to form nanoflakes via a "layer compression" before the curling and re-folding of layered MnO_2 nanosheets occurred. This mechanism is quite different from the proposed mechanisms for structural transitions of δ-MnO_2 previously.[22, 25] This careful control over such structural changes also allowed us to precisely tune the interfacial interaction between AuNPs and MnO_2 that dominates the electrocatalytic activity of MnO_2. The strongly interacted MnO_2 nanosheets and AuNPs could enhance the electrocatalytic activity of MnO_2 roughly 30-40 times.

2. Experimental

2.1 Materials. Potassium permanganate ($KMnO_4$, >99%), gold chloride hydrate ($HAuCl_4$, 99.999%), trisodium citrate, and sodium borohydride ($NaBH_4$, >99%) were purchased from Sigma-Aldrich and used without further purification unless otherwise noted. Deionized water (High-Q, Inc. 103S Stills) with a resistivity of >10.0 MΩ was used in all experiments. All chemical reagents were used without further purification unless otherwise noted.

2.2 Synthesis of AuNP@MnO_2

Preparation of AuNP@MnO_2 nanosheets. In a typical experiment (using AuNP-14 nm an example), 20 mL of $KMnO_4$ (10 mM) were slowly added to 80 mL of as-made AuNP-14 nm solution (the content of sodium citrate is ~24 mg), and incubated under room temperature for 1 h. Then, the above solution was heated to 80 ^oC and incubated for another 30 min to grow monodispersed AuNP@MnO_2 nanosheets. After that, the nanocatalysts were collected by centrifugation twice and washed by water to remove unreacted $KMnO_4$. The as-obtained AuNP@MnO_2 nanosheets were redispersed into water to form 0.2 mg/mL of solution for controlled synthesis of nanoflakes and nanorods. AuNP@MnO_2 nanosheets with different diameters of AuNPs were synthesized according to the above-mentioned procedures.

Hydrothermal treatment of AuNP@MnO_2 nanosheets. AuNP@MnO_2 nanoflakes, curled nanoflakes and nanorods were synthesized by a hydrothermal treatment of AuNP@MnO_2 nanosheets. For AuNP@MnO_2 nanoflakes, the as-prepared solution of AuNP@MnO_2 nanosheets (15 mL) was sealed in Teflon-lined stainless steel autoclaves (25 mL) and hydrothermally treated under 110 ^oC for 6h. After cooled down to room temperature, the product was washed with water for three times. The resulting product was AuNP@MnO_2 nanoflakes (Fig. 2a). Similarly, curled AuNP@MnO_2 nanoflakes were prepared by hydrothermal treatment of AuNP@MnO_2 nanosheets at 135 ^0C for 12 h (Fig. 2c), while AuNP@MnO_2 nanorods were obtained by hydrothermal treatment of AuNP@MnO_2 nanosheets at 160 ^0C for 12 h (Fig. 2e).

2.3 ORR evaluation. The electrocatalytic activities of carbon black, AuNP@MnO_2 nanocatalysts and commercial Pt/C towards oxygen reduction reaction (ORR) were recorded in 0.1 M KOH solution with a rotating disc working electrode (RDE) configuration at room temperature. Pyrolytic graphite (PG) was used as both working and counter electrodes, and a standard calomel electrode was used as a reference electrode. An ink of the nanocatalyst was prepared by mixing 4 mg of catalyst, 1 mg of carbon black (VulcanXC-72) with 1 ml of water/EtOH (1:1). After sonication for 5 min, 85 µL of Nafion solution (5% by wt. in alcohol and water mixture) was further mixed and sonicated for 30 min. The final weight percentages of catalysts, carbon black, and Nafion were 43.3%, 10.8%, 45.9%, respectively. Then 10 µL of above-prepared solution was dropped on the PG working electrode and dried before use. The surface area of the PG working electrode is 0.16 cm^2. The catalysts loading is ~0.24 mg/cm^2 for all samples. The same procedure was used with the commercial Pt/C, but without the addition of carbon black.

The number of electron transferred (n) was calculated according to the Koutecky-Levich (K-L) equation by rotating the electrode at different rates:

$$\frac{1}{J} = \frac{1}{J_L} + \frac{1}{J_k} = \frac{1}{B\omega^{1/2}} + \frac{1}{J_k}$$

$$B = 0.62nFC_0(D_0)^{2/3}\nu^{-1/6}$$

$$J_k = nFkC_0$$

where j is the measured current density, j_k is the kinetic current, and j_L is the diffusion limiting current, respectively. ω is the rotation speed of the electrode in rpm, k is the electron transfer rate constant, B is the reciprocal of the slope of the K-L plots, F is Faraday constant (96485 C/mol), C_0 is the saturated concentration of oxygen in 0.1 M KOH (1.2×10^{-6} mol/cm^3), D_0 is the diffusion coefficient of O_2 (1.9×10^{-5} cm^2/s), and ν is kinematic viscosity of the electrolyte (0.01 cm^2/s).

2.4 Characterizations. SEM images of the nanocatalysts were recorded using a FEI Nova NanoSEM 450 with an accelerating voltage of 10 kV and a beam current of 10 mA. SEM samples were prepared by casting the suspension of the materials on a silicon wafer. TEM and high-resolution TEM (HR-TEM) studies were carried out using a JEOL 2010 TEM with an accelerating voltage of 200 kV. Scanning TEM (STEM) mapping and HAADF-STEM were performed on a Talos F200X Atomic Resolution Analytical Microscope. TEM and STEM samples were prepared by casting the suspension of the materials on a carbon coated copper grid (400 mesh). The wide-angle X-ray scattering (XRD) patterns were recorded using a Rigaku Ultima IV diffractometer (Cu Kα radiation, λ=1.5406 Å) with an operating voltage of 40 kV and a current of 44 mA. Wide-angle XRD were collected over a 2ϑ range of 8~80^o with a continuous scan rate of 0.5^o min^{-1}. Ultraviolet-Visible (UV-vis) spectra were collected with a Cary 60 UV-Vis spectrophotometer. Atomic force microscopy (AFM) was performed on Bruker MultiMode 8 using tapping mode at room temperature. AFM samples were prepared on freshly cleaved mica substrate. X-ray photoelectron (XPS) spectra were recorded on a PHI model 590 spectrometer with multi-probes using Al Kα (λ = 1486.6 eV) as the radiation source. The spectra were recorded in the

View Article Online
DOI: 10.1039/C6TA02017H

fixed analyzer transmission mode with pass energies of 100 and 50 eV for recording survey and high-resolution spectra, respectively. The powder samples were pressed on a carbon tape mounted on an adhesive Cu tape stuck to a sample stage placed in the analysis chamber. Binding

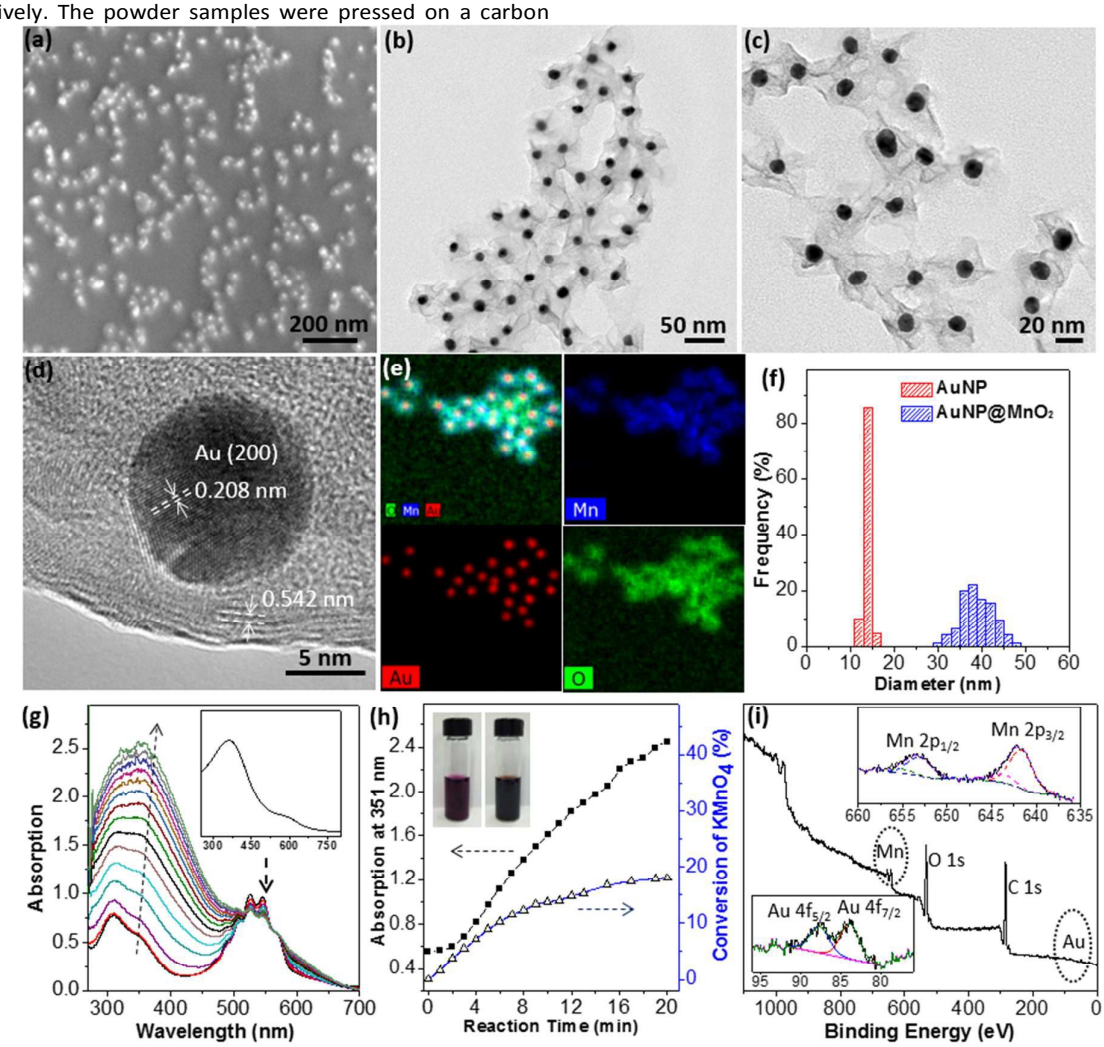

Fig. 1 The nanostructures of AuNP@MnO_2 nanosheets. (a) SEM, (b-c) TEM, (d) HR-TEM images, and (e) STEM-EDX mapping of AuNP@MnO_2 nanosheets. (f) The size distributions of AuNPs and AuNP@MnO_2 nanosheets measured from TEM images by averaging >200 particles. (g) The change in UV-vis absorption of AuNP-$KMnO_4$ solution at various reaction times during synthesis. The UV-vis spectra were recorded at a time interval of 2 mins. The inset of (g) is the UV-vis spectrum of purified AuNP@MnO_2 nanosheets in water. (h) The change of peak intensity at 351 nm (square) and the conversion of $KMnO_4$ (triangle) *vs.* the reaction time. The inset in (h) are the optical pictures of reaction mixtures before (left), and after (right) hydrothermal treatment. (i) XPS spectrum of AuNP@MnO_2 nanosheets and zoomed-in view of Au 4f and Mn 2p peaks.

energies (BEs) were measured for C 1s, O 1s, Au 4f and Mn 2p. The XPS spectra obtained were analyzed and fitted using CasaXPS software (version 2.3.12). Sample charging effects were eliminated by correcting the observed spectra with the C 1s BE value of 284.6 eV. The overlapping Mn 2p and O 1s peaks were deconvoluted into several sub-bands by using an optimal combination of Gaussian (70%) and Lorentzian (30%) functions. Raman measurements were performed using a Renishaw 2000 Raman scope attached to a charge-coupled device camera, with an Ar ion laser (514.4 nm) as the excitation source. The atomic absorption spectroscopy (AAS) measurements were performed using an Atomic Absorption Spectrometer Varian Spectra AA 110. The Au@MnO_2 samples (10 mg) were first digested in an acid solution (HCl : HNO_3 = 3:1, vol) for 10 h until the solids were completely dissolved. The solutions were then diluted with DI water and analyzed by AAS.

3. Results and Discussion

AuNP@MnO_2 nanosheets were prepared using a hydrothermal reduction of $KMnO_4$. In a typical synthesis, the pre-synthesized AuNPs capped with sodium citrate ligands were directly mixed with a $KMnO_4$ solution and hydrothermally treated at 80 ^{o}C for

View Article Online
DOI: 10.1039/C6TA02017H

30 min (see Experimental for synthetic details). As citrate ligands on the surface of AuNPs can act as reductants for MnO_4^-, the color of the mixture solution quickly changed from deep purple to dark brown (inset in Fig. 1h and Fig. S1), indicating the formation of MnO_2 nanosheets. Using 14 nm AuNPs as an example, the growth of MnO_2 nanosheets on the surface of AuNPs was characterized by SEM and TEM as given in Fig. 1 (see Figs. S2-4 for more images). AuNP@MnO_2 nanosheets have a homocentric core-shell nanostructure in which a monodispersed AuNP is uniformly covered by a shell of MnO_2 nanosheets (Fig. 1a-c). The STEM energy-dispersive X-ray (EDX) mapping confirmed the nanostructure and elemental distributions of AuNP@MnO_2 nanosheets. A dense MnO_2 shell grew and fully covered the surface of AuNPs (Fig. 1e). The weight percentage of MnO_2 nanosheets is ~58 wt% from STEM-EDX mapping (Fig. S4), in good consistency with the AAS measurements (Table S1). The MnO_2 shell is composed of multilayered nanosheets (roughly 4-7 layers) as seen in the HR-TEM image (Fig. 1d), corresponded to a thickness of 2~4 nm. The lamellar *d*-spacing of nanosheets from the HR-TEM image is approximately 0.54 nm. The diameter of AuNP@MnO_2 nanosheets is 38±8 nm (Fig. 1f) with a fairly uniform coverage on individual AuNPs. The wrinkles of MnO_2 nanosheets and the centralized location of AuNPs as projected from TEM images suggest that the MnO_2 nanosheets are loosely packed on the surface of AuNPs. XPS of AuNP@MnO_2 nanosheets clearly shows Mn 2p peaks and Au 4f peaks (Fig. 1i). The intensity of Au 4f peaks, however, is much weaker compared to that of Mn 2p peaks, indicating that AuNPs are likely embedded in MnO_2 nanosheets.

The key to growing MnO_2 nanosheets on an individual AuNP is the utilization of citrate-protected AuNPs as a nucleation center. The trace amount of sodium citrate on the AuNP surface can act as a reducing agent for $KMnO_4$.[18, 26] No additional reducing agents were required in our synthesis system. The reduction of $KMnO_4$ likely occurred heterogeneously only on the surface of AuNPs, as no free MnO_2 nanosheets were observed from TEM images. To monitor the conversion of $KMnO_4$ and formation process of MnO_2 nanosheets along AuNPs, time-dependent UV-Vis spectra of the reaction mixture were recorded (Fig. 1g). The initial UV-vis absorption peaks at around 310 nm and 560 nm are attributed to the absorption of MnO_4^-. The gradual decrease in intensity at 560 nm can be seen when incubating at 80 °C. Meanwhile, a new broad peak at ~351 nm appeared; its intensity increased rapidly, indicating the formation of colloidal MnO_2 nanosheets.[27] The kinetic change of the peak intensity at 351 nm and the conversion of $KMnO_4$ calculated from the absorption peak at 560 nm were given in Fig. 1h. The conversion of $KMnO_4$ could only reach up to ~19% regardless of the reaction time. This low conversion suggests the amount of $KMnO_4$ was excessive and the formation of MnO_2 nanosheets was only dependent on the "insufficient" amount of sodium citrate ligands on AuNPs. Once the surface was completely consumed, the growth of MnO_2 nanosheets should have ceased. Furthermore, the diameter of MnO_2 nanosheets (as the shell) is insensitive to the original sizes of AuNP cores. With sodium citrate as the capping ligands of AuNPs, this synthetic method was demonstrated to grow 2-D core-shell AuNP@MnO_2 nanosheets with 4-45 nm AuNP cores (Fig. S5-7). Interestingly, the diameter of MnO_2 nanosheets on the surface of AuNPs remained in the range of 12-18 nm regardless of AuNP sizes. Again, the importance of limited reducing agents on AuNP is to avoid the overgrowth of nanosheets.

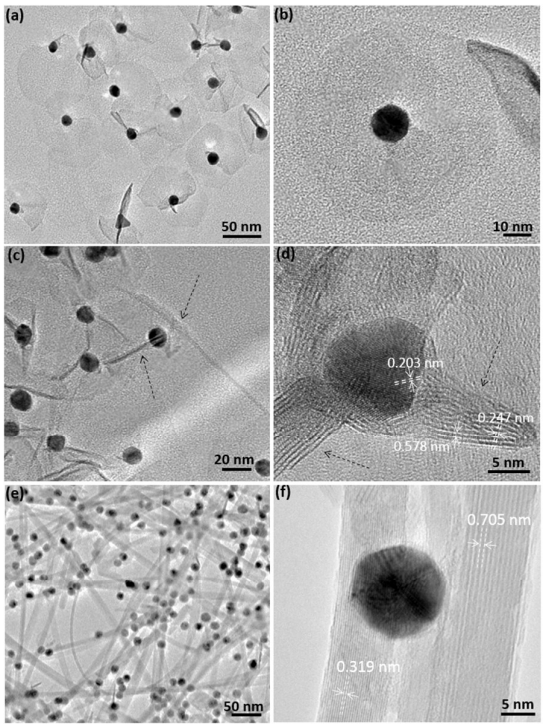

Fig. 2 The morphological evolutions of AuNP@MnO_2 nanosheets under different hydrothermal temperatures. TEM images of MnO_2 nanomaterial transformed from (a,b) 2-D MnO_2 nanoflakes with near hexagonal morphology, to (c,d) curled nanoflakes with partially folding nanotubes/nanorods, and eventually to (e,f) 1-D nanorods. The arrows in (c-d) indicate the curling and folding of MnO_2 nanoflakes.

When subjected to a hydrothermal treatment, the morphological evolution of MnO_2 nanosheets can be recorded using electron microscopy (Fig. 2). Taking 14-nm AuNP@MnO_2 nanosheets as an example again, upon the hydrothermal treatment at 110 °C for 6 hr, randomly stacked MnO_2 nanosheets gradually spread out and became rigid, near-hexagonal nanoflakes (Fig. 2b). The diameter of 2-D nanoflakes increased to ~80 nm (Fig. S8-10), approximately two times larger in diameter, compared to that of the initial nanosheets; while, the thickness of nanoflakes decreased to ~1.4 nm (Fig. S9), corresponding to 2~3 atomic layers of MnO_2 layered nanosheets. During this process, AuNPs migrated toward the edge of the nanoflakes; and the curling/folding of the nanoflakes could be also seen from the edges of nanoflakes. When increasing the temperature to 135 °C for 12 hr, a large decrease in diameter of MnO_2 nanoflakes can be observed from the TEM images (Fig. 2c-d and Fig. S11). AuNPs were off-

View Article Online
DOI: 10.1039/C6TA02017H

center mostly. The edges of nanoflakes partially curled and refolded into 1-D rod-like morphologies (3~5 nm in diameter). The increase in diameter of 1-D rods was likely due to the multiple curling and folding at the edges as shown in Fig. 2d. The layer spacing of nanoflakes slightly increased to 0.578 nm. The lattice fringe of 0.247 nm perpendicular to the layers can be assigned to the (211) plane of α-MnO_2, indicating that layered Birnessite δ-MnO_2 has partially evaluated into α-MnO_2. With further increasing the hydrothermal temperature to 160 ^oC, the curled nanoflakes merged together through interparticle recrystallization. Long MnO_2 nanorods with a diameter of 10-20 nm and a length up to several micrometers were observed; while AuNPs completely moved to the surface of the MnO_2 nanorods (Fig.2e-f). The two *d*-spacings of 0.705 nm and 0.319 nm were seen for MnO_2 nanorods under HR-TEM, corresponding to the (110) and (310) planes of α-MnO_2, respectively (Fig. 2f). A slight loss of AuNPs was noted during the phase transitions of MnO_2 as given in Table S1. It is possibly because of the migration of AuNPs to the surface of MnO_2. Some of weakly interacted AuNPs were removed during the sample purification.

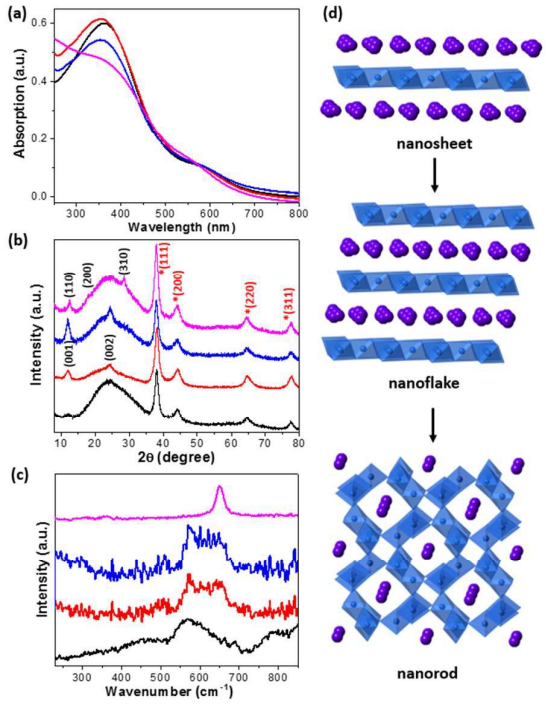

Fig. 3 The structural evolutions of AuNP@MnO_2 nanosheets. (a) UV-vis spectra, (b) XRD patterns and (c) Raman spectra for nanosheets (black), nanoflakes (red), curled nanoflakes (blue) and nanorods (magenta). The diffraction peaks from polycrystalline gold in (b) are marked with "*". (d) The change in crystalline structures from amorphous multilayered nanosheets to δ-MnO_2 nanoflakes, and to α-MnO_2 nanorods with tunnel structures.

The structural transitions of MnO_2 nanosheets were further confirmed using UV-vis absorption spectra (Fig. 3a), XRD (Fig. 3b) and Raman scattering spectra (Fig. 3c). First, two absorption peaks of MnO_2 nanosheets could be found, one at ~360 nm for MnO_2 colloids and the other one at 568 nm for the localized surface plasmon absorption of AuNPs. The electronic excitation of MnO_2 layered structures is known to be determined by the interlayer spacing and the size of MnO_2 colloids.[28] The absorption peak of MnO_2 nanosheets at 360 nm firstly blue-shifted to 354 nm (nanoflakes), due to the decrease in the layer number of nanosheets; and then red-shifted to 356 nm (curled nanoflakes), because of the re-curling of nanosheets. The intensity of the absorption peak became weaker with the formation of α-MnO_2 nanorods.[29]

Second, the structural transitions of MnO_2 were further monitored by XRD (Fig. 3b). Four strong XRD peaks in the range of 38-80^o for all samples are ascribed to polycrystalline AuNPs. For AuNP@MnO_2 nanosheets, MnO_2 was absence of regular layer stacking and only a weak, a broad XRD peak was found at ~12.4^o, possibly originating from the lamellar structure of multilayered nanosheets during drying. Two well-defined XRD signals appeared at 12.0^o and 24.4^o for AuNP@MnO_2 nanoflakes, assigned to (001) and (002) reflections of Birnessite-type δ-MnO_2, respectively. For curled AuNP@MnO_2 nanoflakes, the peaks of (001) and (002) reflections did not shift but the intensities of peaks further increase. Thus, both spread nanoflakes and curled nanoflakes are mostly assigned to δ-MnO_2. In the case of AuNP@MnO_2 nanorods, three diffraction peaks were identified as (110), (200), and (310) planes of α-MnO_2. Overall, the structural evolution of MnO_2 nanosheets during the hydrothermal process was confirmed from amorphous layered structures, to δ-MnO_2, and eventually to α-MnO_2 (Fig. 3d).

Raman spectroscopy was used to further probe the change in the molecular vibrational behaviour of materials and support the structural transitions of nanosheets (Fig. 3c). The very initial MnO_2 nanosheets were amorphous, which only exhibited a single broad Raman signal at 572 cm^{-1}. This peak was assigned to the Mn-O lattice vibration of MnO_6 octahedra.[25, 30] A new Raman peak gradually appeared at around 645 cm^{-1} for AuNP@MnO_2 nanoflakes, indicating the formation of Birnessite-type δ-MnO_2 and the stacking of layers. The peak at ~572 cm^{-1} disappeared and only one sharp Raman peak appeared at around 652 cm^{-1}, which confirmed the structural transition to α-MnO_2 nanorods. This suggested the reorganization of MnO_6 octahedra with less lattice distortion after hydrothermal treatment.[30]

The structural transitions of MnO_2 polymorphs, as well as the transition mechanism of 2-D layered structures to 1-D nanorods under hydrothermal treatments, have been reported previously.[22, 23, 25] Wang *et al.* observed the formation of δ-MnO_2 nanosheets as an intermediate to produce 1-D MnO_2 nanostructures.[22] The rolling/curling of layered lamellar structures was proposed for the structural transition. Shen *et al.* studied the phase transformation of Birnessite MnO_2 to β-MnO_2 by *in situ* synchrotron powder XRD.[23] The layer "compression" of re-stacked Birnessite MnO_2 along the *c* direction was

View Article Online
DOI: 10.1039/C6TA02017H

Journal Name

ARTICLE

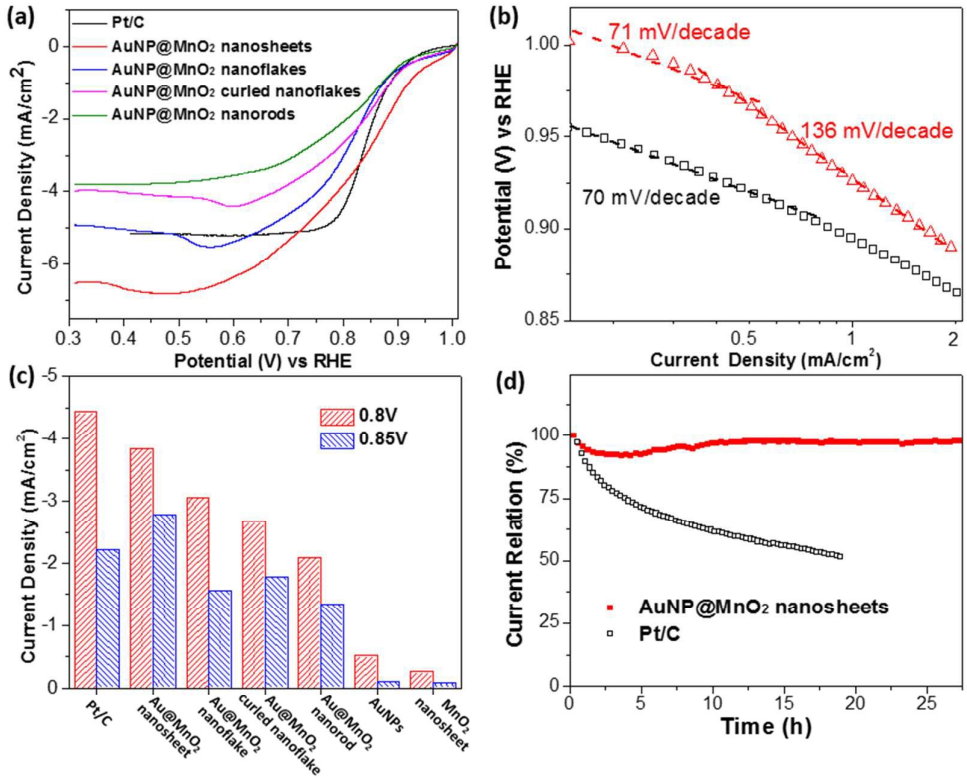

Fig. 4 Electrocatalytic ORR activities of AuNP@MnO_2. (a) LSV curves of commercialized Pt/C (black line) and AuNP@MnO_2. The rotation speed of electrodes is 1600 rpm and the loading amount of AuNP@MnO_2 and Pt/C is 0.24 mg/cm^2. (b) Tafel plots of AuNP@MnO_2 nanosheets (red line) and Pt/C (black line). (c) Current densities of ORR activities at potential of 0.8 V (red) and 0.85 V (blue) of Pt/C, Au@MnO_2, discrete AuNPs and MnO_2 nanosheets. (d) The long-term stability of AuNP@MnO_2 nanosheets (black line) and Pt/C (red line).

experimentally recorded to be responsible for the formation of 1×2 and/or 1×1 tunnel structures. In a very recent report, Sinha *et al*. presented a possible "dissolution-recrystallization" mechanism for the shape transformation of MnO_2 nanosheets to nanowires.[25] They proposed that the dissolution of amorphous δ-MnO_2 nanosheets occurred first to detach and diffuse into nanodomains and further recrystallized on α-MnO_2 nuclei.

Our results likely fit in to the layer "compression" mechanism. The formation of MnO_2 nanoflakes was conceivably a result of the layer "compression" at the *c* direction. The most direct observation is that, the increase in the diameter of nanosheets from 38 to 80 nm and the decrease in layer thickness are evidenced for the remerging of nanosheets at 110 ^{o}C. This process was also associated simultaneously with the formation of tunnel structures of MnO_2 nanorods (2×2 tunnel in this case) perpendicular to the lamella (Fig. 2d). The phase transitions of MnO_2 were not influenced by the presence of AuNPs (Fig. S13) or the sizes of AuNPs (Fig. S5-7). However, when the size of AuNPs was larger (> 20 nm), the layer "compression" of MnO_2 nanosheets became more difficult, as the transition for core-shell AuNP@MnO_2 nanosheets to nanoflakes involved a larger volume expansion. Overall, aggregation-free MnO_2 nanosheets on the surface of AuNPs made it possible to visualize the structural transitions at a single-NP level.

Since all intermediates of structural evolutions can be isolated using different hydrothermal temperatures, it is thus possible to evaluate the effect of nanostructures and polymorphs of MnO_2 on electrocatalytic activity for the ORR (Fig. 4). To examine ORR activities, cyclic voltammetry (CV) was performed on AuNP@MnO_2 nanosheets (14 nm-AuNPs for all electrochemical results) in 0.1 M KOH solution (Fig. S14). In a N_2-saturated electrolyte, the voltammogram without an

View Article Online
DOI: 10.1039/C6TA02017H

obvious slope for cathodic current density was present; while, a well-defined cathodic oxygen reduction peak with a high current density appeared in an O_2-saturated electrolyte, indicating that the AuNP@MnO_2 nanosheet is active for ORRs. The ORR activity of AuNP@MnO_2 nanosheets was further recorded using linear sweep voltammetric (LSV) scanning with a sweep rate of 5 mV s^{-1}. As a comparison, similar measurements were performed on the commercialized Pt/C catalyst (20 wt% of Pt loaded) (also see Fig. S15 for ORR activity of Vulcan XC-72 carbon black). The ORR current-potential curve of AuNP@MnO_2 nanosheets (0.24 mg/cm^2) shows a lower onset potential and higher current density. The current density at the reduction potential of 0.9 V (*vs.* reversible hydrogen electrode (RHE), hereafter) is -1.41 mA/cm^2 for AuNP@MnO_2 nanosheets, corresponding to a two-fold higher activity than commercialized Pt/C catalysts (-0.82 mA/cm^2). The potential at j = -2 mA/cm^2 for AuNP@MnO_2 nanosheets is 0.88 V, 30 mV higher than that of Pt/C catalysts (Fig. 4a). The stability of AuNP@MnO_2 nanosheets was also studied by current-time (*i*-*t*) chronoamperometry at a constant potential of 0.6 V (Fig. 4d). A respectable current retention of >96% for AuNP@MnO_2 nanosheets was maintained after 24 hr, indicating a superior durability of AuNP@MnO_2 nanosheet catalysts; while only 50% of activity was found for Pt/C catalyst after 19 hr. Moreover, the AuNP@MnO_2 nanosheets also showed a better tolerance to methanol crossover effects (Fig. S20).

Table 1. Summary of the ORR catalytic activities

Catalysts [a]	E_0 (V) [b]	$E_{1/2}$ (V) [b]	$E_{j=-3\ mA/cm2}$ (V) [c]
AuNP@MnO_2 nanosheets	0.92	0.82	0.84
AuNP@MnO_2 nanoflakes	0.88	0.81	0.80
AuNP@MnO_2 curled nanoflakes	0.90	0.83	0.78
AuNP@MnO_2 nanorods	0.92	0.83	0.72
MnO_2 nanosheets	0.86	0.65	n. a.
AuNP (14 nm)	0.86	0.70	n. a.
Pt/C	0.91	0.84	0.83
Vulcan XC-72 carbon	0.75	0.69	n. a.

[a]All catalysts are based on 14 nm AuNP in this investigation. [b]Results based on LSV curves collected on RDE with a rotation rate of 1600 rpm: E_0 is the onset potential; $E_{1/2}$ is the half-wave potential. [c]Potential versus RHE at -3 mA/cm^2. The rotation speed of electrodes is 1600 rpm for all samples.

Tafel plots of AuNP@MnO_2 nanosheets and Pt/C catalyst derived from LSV curves are given in Fig. 4b. In the electron-transfer dominating region (j<1 mA/cm^2), two well-defined linear slopes of -71 mV/decade and -136 mV/decade are present for AuNP@MnO_2 nanosheets. There are likely two kinetic processes occurring on two types of ORR active sites (also see Fig. S18).[31] To gain further insight into the ORR kinetics, the kinetic-limiting current j_k was measured at various rotation speeds and the number of electrons transferred (n) for the ORR calculated from Koutecky-Levich (K-L) plots (Fig. S17). The average number of electron transfer for AuNP@MnO_2 nanosheets is between 3.1 and 2.7 in the potential range of 0.75-0.35 V *vs.* RHE, giving an H_2O_2 yield of 45%~65%; this shows a slight decrease when decreasing the potential. Transition metal oxides generally favor a partial $2e^-$ reduction to form H_2O_2, as these oxides are highly active in alkaline media toward the disproportionation reaction of H_2O_2, especially for layered MnO_2 nanosheets.[31] This implies that the active sites generated by the synergetic coupling of MnO_2 and AuNPs were somehow responsible for the enhanced activity for ORRs.

Several control experiments were carried out to confirm this hypothesis. First, the ORR activities of discrete loose-packed MnO_2 nanosheets and 14-nm AuNPs were examined under the same experimental conditions (Fig. S16 and Table 1). Both of them exhibited a low ORR catalytic activity with a half-wave potential <0.7 V, similar to the reported results.[31, 32] The activity of AuNP@MnO_2 nanosheets is roughly 30-40-fold higher than that of pure MnO_2 nanosheets and 14-nm AuNPs (Fig. 4c). One main reason for the high electrocatalytic activity of AuNP@MnO_2 nanosheets is the decrease of charge transfer resistance, compared to pure MnO_2 nanosheets (Fig. S18-19). Second, the ORR activities of AuNP@MnO_2 nanoflakes, curled nanoflakes and nanorods were also evaluated (Fig. 4a) under similar conditions. All ORR polarization curves shifted to lower potentials when increasing the hydrothermal temperatures. The potential to reach j = -3 mA/cm^2 is 0.80 V for nanoflakes, 0.78 V for curled nanoflakes and 0.72 V for nanorods, respectively, indicating a drop of ORR activity over the course of morphological transitions. The morphological transition from nanosheets to nanorods of AuNP@MnO_2 resulted in a 50% loss of activity at the potentials of 0.8 V and 0.85 V (Fig. 4c).

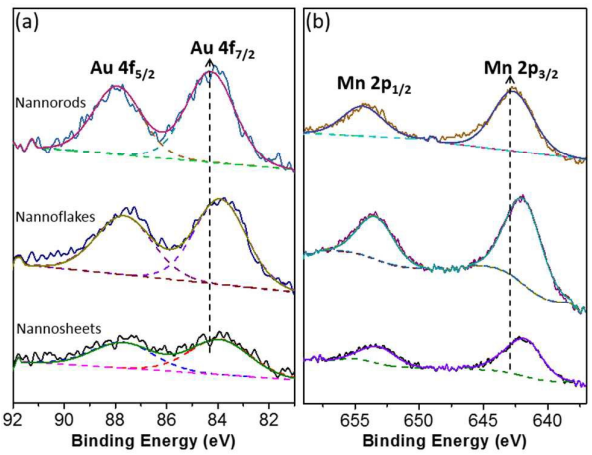

Fig. 5 Au 4f (a) and Mn 2p (b) XPS spectra of AuNP@MnO_2.

Many previous studies have demonstrated that α-MnO_2 has the best ORR activity among all polymorphs of MnO_x.[33-36] For pure MnO_2 catalysts, the initial step of electrochemical reduction of MnO_2 *via* the breaking of oxo bridges and proton insertion of edge-shared MnO_6 octahedra is important in terms of the formation of active Mn sites for the O_2 bonding.[37]

View Article Online
DOI: 10.1039/C6TA02017H

The stronger Mn-O bonding strength generally makes the initial proton insertion process more difficult. The average Mn-O bond length of layered MnO_2 is in the range of 0.191~0.194 nm,[38] smaller than that of α-MnO_2 nanorods. This suggests that the oxo bridges in α-MnO_2 nanorods are easier for proton insertion, in terms of the bonding energy, leading to a higher ORR activity for α-MnO_2 nanorods, in principle. Therefore, these results, again, point out that the enhanced ORR activity of AuNP@MnO_2 nanosheets is a result of the interaction of AuNPs and MnO_2 nanosheets. The synergetic effect from the interaction of MnO_2 nanosheets and AuNPs is responsible for the ORR activity of AuNP@MnO_2 nanosheets.

We further used XPS spectra to characterize the interaction of AuNPs and MnO_2 nanosheets. The high-resolution XPS spectra of Au 4f and Mn 2p regions of AuNP@MnO_2 nanosheets, nanoflakes and nanorods are given in Fig. 5. The Au $4f_{7/2}$ peak with a binding energy of ~84.3 eV for AuNP@MnO_2 nanorods indicates a metallic Au(0) state (Fig. 5(a)). The decrease of Au $4f_{7/2}$ binding energy ~0.3 eV and the broadening of Au $4f_{7/2}$ peak can be seen for AuNP@MnO_2 nanosheets. This shift in the binding energy is interpreted as a result of the presence of partial positive Au^+ species, because of the strong adsorption of AuNPs on the oxygen vacancies of MnO_2 nanosheets *via* strong electronic interactions.[39, 40] For AuNP@MnO_2 nanosheets, the formation of Au^+ species is likely due to the over oxidation of Au atoms on the surface of AuNPs by $KMnO_4$; while, these Au^+ species can be reduced by Mn species with a lower oxidation state at elevated temperatures during hydrothermal treatments. As a comparison, the binding energy of Mn $2p_{3/2}$ peak appears at ~641.8 eV for AuNP@MnO_2 nanosheets, and gradually shifts to ~642.7 eV for AuNP@MnO_2 nanorods. A lower binding energy of Mn 2p peaks (~0.9 eV) is observed for AuNP@MnO_2 nanosheets. This suggests that a higher proportion of Mn species with a lower oxidation state existed in AuNP@MnO_2 nanosheets. It should be pointing out that the formation of Mn species with a lower oxidation state was a result of the interfacial interaction of AuNPs and MnO_2 nanosheets, other than the change of K^+. No change in oxidation state was observed without the presence of AuNPs in our control experiments (Fig. S13) and in another similar report.[25] The nature of interaction between MnO_x with AuNPs is currently unclear and further work is still undergoing.

The enhancement of the ORR activity for AuNP@MnO_2 nanosheets is possibly attributed to the promotion of positive Au^+ species, known as metal-oxide interfacial interaction. The interaction of positive Au^+ species and surface oxygen can largely weaken Mn-O bonds,[41-43] thus leading to the formation of extremely active sites for ORRs. The reduction of Au^+ species after hydrothermal treatments possibly weakened the metal-oxide interaction. This is particularly supported by the migration of AuNPs toward the surface of MnO_2 when the morphological transitions occurred. It thus led to the decrease of electrocatalytic activity.

4. Conclusions

To summarize, we described a facile synthesis of AuNP@MnO_2 nanosheets and studied their structural and morphological transitions under hydrothermal treatment. Unconventional morphological transitions of MnO_2 nanosheets to α-MnO_2 nanorods were observed using electron microscopy at a single-NP level. The layer "compression" of 2-D layered MnO_2 nanosheets was proposed to be responsible for the formation of MnO_2 nanoflakes as an intermediate. We have demonstrated that the strongly interacted AuNPs and MnO_2 could significantly enhance their electrocatalytic activity for the ORR. The partially oxidized Au^+ resulted in a strong interaction at the metal-oxide interface and therefore the improvement of the ORR activity for 30-40 fold. The insight into the effect of the topological nanostructures and metal-oxide interactions on the electrocatalytic performance of MnO_x family may illustrate an alternative pathway to develop new electrocatalysts.

Acknowledgements

JH thanks the financial support of startup funds from the University of Connecticut. SLS acknowledges support of the US Department of Energy, Office of Basic Energy Sciences, Division of Chemical, Biological and Geological Sciences under grant DE-FG02-86ER13622. A000. The SEM/TEM studies were performed using the facilities in the UConn/FEI Center for Advanced Microscopy and Materials Analysis (CAMMA). This work was also partially supported by the Green Emulsions Micelles and Surfactants (GEMS) Center, FEI Company under an FEI-UConn partnership agreement and a Research Excellence Award of the University of Connecticut.

Notes and references

1. R. Ma and T. Sasaki, *Adv. Mater.*, 2010, **22**, 5082-5104.
2. H. Zhang, *ACS nano*, 2015, **9**, 9451-9469.
3. X. Zhuang, Y. Mai, D. Wu, F. Zhang and X. Feng, *Adv. Mater.*, 2015, **27**, 403-427.
4. M. Yang, Y. Hou and N. A. Kotov, *Nano Today*, 2012, **7**, 430-447.
5. Y. Y. Liang, Y. G. Li, H. L. Wang, J. G. Zhou, J. Wang, T. Regier and H. J. Dai, *Nat. Mater.*, 2011, **10**, 780-786.
6. M. R. Gao, Y. F. Xu, J. Jiang, Y. R. Zheng and S. H. Yu, *J. Am. Chem. Soc.* , 2012, **134**, 2930-2933.
7. H. X. Zhong, J. Wang, Y. W. Zhang, W. L. Xu, W. Xing, D. Xu, Y. F. Zhang and X. B. Zhang, *Angew. Chem. Int. Ed.*, 2014, **53**, 14235-14239.
8. S. Guo and S. Sun, *J. Am. Chem. Soc.* , 2012, **134**, 2492-2495.
9. S. Guo, S. Zhang, L. Wu and S. Sun, *Angew. Chem. Int. Ed.*, 2012, **51**, 11770-11773.
10. M. Gong, Y. Li, H. Wang, Y. Liang, J. Z. Wu, J. Zhou, J. Wang, T. Regier, F. Wei and H. Dai, *J. Am. Chem. Soc.* , 2013, **135**, 8452-8455.
11. S. Gao, Y. Lin, X. Jiao, Y. Sun, Q. Luo, W. Zhang, D. Li, J. Yang and Y. Xie, *Nature*, 2016, **529**, 68-71.
12. S. L. Suib, *Acc. Chem. Res.*, 2008, **41**, 479-487.
13. Y. Omomo, T. Sasaki, L. Wang and M. Watanabe, *J. Am. Chem. Soc.* , 2003, **125**, 3568-3575.
14. C. Wei, L. Yu, C. Cui, J. Lin, C. Wei, N. Mathews, F. Huo, T. Sritharan and Z. Xu, *Chem. Commun.*, 2014, **50**, 7885-7888.

View Article Online
DOI: 10.1039/C6TA02017H

15. N. Ohno, Y. Akeboshi, M. Saito, J. Kuwano, H. Shiroishi, T. Okumura and Y. Uchimoto, *Top. Catal.*, 2009, **52**, 903-911.
16. Z. Liu, K. Xu, H. Sun and S. Yin, *Small*, 2015, **11**, 2182-2191.
17. Y. L. Ding, Y. Wen, P. A. van Aken, J. Maier and Y. Yu, *Small*, 2015, **11**, 2011-2018.
18. L. Wei, C. Li, H. Chu and Y. Li, *Dalton Trans.*, 2011, **40**, 2332-2337.
19. G. Zhao, J. Li, L. Jiang, H. Dong, X. Wang and W. Hu, *Chemical Science*, 2012, **3**, 433-437.
20. S. Chen, J. Zhu, X. Wu, Q. Han and X. Wang, *ACS nano*, 2010, **4**, 2822-2830.
21. F. Cheng and J. Chen, *Chem Soc Rev*, 2012, **41**, 2172-2192.
22. X. Wang and Y. Li, *Chem. Eur. J.*, 2003, **9**, 300-306.
23. X.-F. Shen, Y.-S. Ding, J. C. Hanson, M. Aindow and S. L. Suib, *J. Am. Chem. Soc.* , 2006, **128**, 4570-4571.
24. T. T. Truong, Y. Liu, Y. Ren, L. Trahey and Y. Sun, *ACS nano*, 2012, **6**, 8067-8077.
25. A. K. Sinha, M. Pradhan and T. Pal, *J. Phys. Chem. C*, 2013, **117**, 23976-23986.
26. J. Turkevich, P. C. Stevenson and J. Hillier, *Discuss. Faraday Soc.*, 1951, **11**, 55-75.
27. K. Okitsu, M. Iwatani, B. Nanzai, R. Nishimura and Y. Maeda, *Ultrason. Sonochem.*, 2009, **16**, 387-391.
28. S. L. Brock, M. Sanabria, S. L. Suib, V. Urban, P. Thiyagarajan and D. I. Potter, *J. Phys. Chem. B*, 1999, **103**, 7416-7428.
29. W. Li, X. Cui, R. Zeng, G. Du, Z. Sun, R. Zheng, S. P. Ringer and S. X. Dou, *Sci. Rep.*, 2015, **5**, 8987.
30. A. Iyer, J. Del-Pilar, C. K. King'ondu, E. Kissel, H. F. Garces, H. Huang, A. M. El-Sawy, P. K. Dutta and S. L. Suib, *J. Phys. Chem. C*, 2012, **116**, 6474-6483.
31. W. Xiao, D. Wang and X. W. Lou, *J. Phys. Chem. C*, 2009, **114**, 1694-1700.
32. M. S. El-Deab, T. Sotomura and T. Ohsaka, *Electrochem. Commun.*, 2005, **7**, 29-34.
33. Y. Meng, W. Song, H. Huang, Z. Ren, S. Y. Chen and S. L. Suib, *J. Am. Chem. Soc.* , 2014, **136**, 11452-11464.
34. F. Cheng, Y. Su, J. Liang, Z. Tao and J. Chen, *Chem Mater*, 2009, **22**, 898-905.
35. W. Xiao, D. Wang and X. W. Lou, *J. Phys. Chem. C*, 2010, **114**, 1694-1700.
36. Y. Gorlin and T. F. Jaramillo, *J Am Chem Soc*, 2010, **132**, 13612-13614.
37. C.-H. Kuo, I. M. Mosa, S. Thanneeru, V. Sharma, L. Zhang, S. Biswas, M. Aindow, S. P. Alpay, J. F. Rusling, S. L. Suib and J. He, *Chem Commun*, 2015, **51**, 5951-5954.
38. K. Fukuda, I. Nakai, Y. Ebina, M. Tanaka, T. Mori and T. Sasaki, *J. Phys. Chem. B*, 2006, **110**, 17070-17075.
39. N. Kruse and S. Chenakin, *Appl. Catal. A: Gen.*, 2011, **391**, 367-376.
40. B. Liu, C. H. Kuo, J. Chen, Z. Luo, S. Thanneeru, W. Li, W. Song, S. Biswas, S. L. Suib and J. He, *Angew. Chem. Int. Ed.*, 2015, **54**, 9061-9065.
41. C.-H. Kuo, W. Li, L. Pahalagedara, A. M. El-Sawy, D. Kriz, N. Genz, C. Guild, T. Ressler, S. L. Suib and J. He, *Angew. Chem. Int. Ed.*, 2015, **54**, 2345-2350.
42. Y. Gorlin, C.-J. Chung, J. D. Benck, D. Nordlund, L. Seitz, T.-C. Weng, D. Sokaras, B. M. Clemens and T. F. Jaramillo, *J. Am. Chem. Soc.*, 2014, **136**, 4920-4926.
43. A. K. Sinha, K. Suzuki, M. Takahara, H. Azuma, T. Nonaka and K. Fukumoto, *Angew. Chem. Int. Ed.*, 2007, **46**, 2891-2894.

View Article Online
DOI: 10.1039/C6TA02017H

Table of Contents

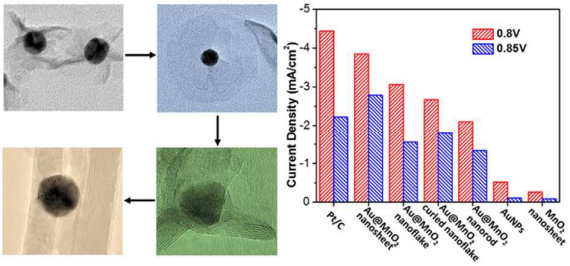

A facile approach to growing two-dimensional MnO_2 nanosheets on gold nanoparticles is reported.